Gut Clostridium sporogenes-derived indole propionic acid suppresses osteoclast formation by activating pregnane X receptor

Feng Li（✉ lifengmd@hust.edu.cn）

 Tongji Hospital, Tongji Medical College, Huazhong University of Science and Technology, Wuhan

Renpeng Peng

 Tongji Hospital, Tongji Medical College, Huazhong University of Science and Technology

Chao Song

 Tongji Hospital, Tongji Medical College, Huazhong University of Science and Technology

Shuangquan Gou

 Tongji Hospital, Tongji Medical College, Huazhong University of Science and Technology

Haiyang Liu

 Tongji Hospital, Tongji Medical College, Huazhong University of Science and Technology

Honglei Kang

 Orthopedics, Tongji Medical College, Huazhong University of Science and Technology, Wuhan

Yimin Dong

 Orthopedics, Tongji Medical College, Huazhong University of Science and Technology, Wuhan

Yong Xu

 Tongji Hospital, Tongji Medical College, Huazhong University of Science and Technology

Peixuan Hu

 Tongji Hospital, Tongji Medical College, Huazhong University of Science and Technology

Kaiyong Cai

 Key Laboratory of Biorheological Science and Technology, Ministry of Education, College of Bioengineering, Chongqing University

Qian Feng

 Key Laboratory of Biorheological Science and Technology, Ministry of Education, College of Bioengineering, Chongqing University

Hanfeng Guan

 Tongji Hospital, Tongji Medical College, Huazhong University of Science and Technology

Article

Keywords:

Additional Declarations: (Not answered)

Abstract

Bone homeostasis is maintained by osteoclast-mediated bone resorption and osteoblast-mediated bone formation. A dramatic decrease in estrogen levels in postmenopausal women leads to osteoclast overactivation, impaired bone homeostasis, and subsequent bone loss. Changes in the gut microbiome affect bone mineral density. However, the role of the gut microbiome in estrogen deficiency-induced bone loss remains unknown. In this study, we found that the abundance of *Clostridium sporogenes* (*C. spor.*) and its derived metabolite, indole propionic acid (IPA), were decreased in ovariectomized (OVX) mice. *In vitro* assays suggested that IPA suppressed osteoclast differentiation and function. At the molecular level, IPA suppressed receptor activator of nuclear factor kappa-B ligand-induced pregnane X receptor (PXR) ubiquitination, leading to the degradation of PXR and release of its binding p65. *In vivo* daily IPA administration or repeated *C. spor.* colonization protected against OVX-induced bone loss. To protect live bacteria from the harsh gastric environment and delay the emptying of orally administered *C. spor.* from the intestine, a *C. spor.*-encapsulated silk fibroin (SF) hydrogel system was developed, which achieved bone protection in OVX mice comparable to that achieved with repeated germ transplantation or daily IPA administration. Overall, we found that gut *C. spor.*-derived IPA was involved in estrogen deficiency-induced osteoclast overactivation by regulating the PXR/p65 complex. The *C. spor.*-encapsulated SF hydrogel system is a promising tool for combating postmenopausal osteoporosis without the disadvantages of repeated germ transplantation.

Introduction

The balance between osteoclast-mediated bone resorption and formation is critical for maintaining bone homeostasis. Excessive bone resorption is involved in pathological bone loss in diseases such as postmenopausal osteoporosis, Paget's bone disease, and periprosthetic osteolysis. Osteoclasts are derived from monocyte/macrophage lineage cells under the stimulation of two major cytokines—macrophage colony-stimulating factor (M-CSF) and receptor activator of nuclear factor kappa-B ligand (RANKL). M-CSF activates c-Fms to promote the proliferation and differentiation of monocytes into macrophages. RANKL binds to receptor activator of nuclear factor kappa-B (RANK) on the cell surface, and tumor necrosis factor receptor-associated factor 6 (TRAF6) is subsequently recruited to the inner cellular domain of RANK. p62 binds to TRAF6 and interacts with atypical protein kinase C (PKC), followed by IκB kinase (IKK) complex activation [1]. Alternatively, TRAF6 forms a complex with transforming growth factor-β-activated kinase 1 (TAK1), which phosphorylates the IKK complex [2]. This complex subsequently phosphorylates IκB, leading to its proteasome-mediated degradation and nuclear translocation of free p65/RelA and p50 to the nucleus, resulting in the activation of master transcription factors essential for osteoclast differentiation [3]. RelA/p65 has been identified to inhibit c-Jun N-terminal kinase (JNK)-mediated apoptosis, and the absence of RelA/p65 results in a deficient osteoclastogenic response to RANKL. Furthermore, M-CSF and RANKL both activate mitogen-activated protein kinases (MAPKs), including extracellular signal-regulated kinase 1/2 (ERK1/2), JNK1/2/3, and p38, which are essential for osteoclast differentiation [4].

Homeostasis of the gut microbiome is essential for health. Recent evidence indicates that deviations in the gut microbiota are associated with abnormal bone mineral density. Using shotgun metagenomic sequencing, unclassified *Clostridia* and *Methanobacteriaceae* were found to be more abundant in osteoporotic and osteopenic postmenopausal women than in healthy controls [5]. Another study demonstrated that the abundances of *Proteobacteria* and *Synergistetes* were higher, whereas those of *Bacteroidetes* were lower at the phylum level in the postmenopausal osteopenia group than in the control group [6]. Other studies have demonstrated that probiotics are beneficial for bone health in postmenopausal women [7].

In animal models, germ-free mice exhibited increased bone mineral density associated with a reduced number of osteoclasts per bone surface compared with conventionally raised mice [8]. Another study demonstrated that colonization by conventional specific pathogen-free gut microbiota increased both bone formation and resorption in germ-free mice by upregulating insulin-like growth factor-1 (IGF-1). Supplementation of antibiotic-treated mice with short-chain fatty acids (SCFAs), which are products of microbial metabolism, restored IGF-1 and bone mass to the levels observed in control mice [9]. In addition to SCFAs, various gut microbiome-derived metabolites such as bile acids [10], branched-chain amino acids [11,12], and trimethylamine N-oxide [13] have been implicated in regulating bone homeostasis. However, the functions of tryptophan and its derivative indoles in bones remain unknown.

Tryptophan is an essential amino acid in humans that is supplied through diet. Several bacterial species convert tryptophan into indole and indole derivatives [14]. Tryptophan is converted to indole by tryptophanase (TnaA), which is expressed in bacterial species, including *Escherichia coli, Clostridium* spp., and *Bacteroides* spp. In addition, *Clostridium sporogenes* (*C. spor.*) converts tryptophan into tryptamine, indole lactic acid (ILA), and 3-indole propionic acid (IPA) using tryptophan aminotransferase. *Clostridium* spp. colonize the large intestine, particularly the mucosal folds of the ascending colon [15]. Another group of bacteria capable of converting tryptophan is *Lactobacillus spp.*, which converts tryptophan to indolealdehyde (IAld) and ILA via aromatic amino acid aminotransferase (ArAT) and indolelactic acid dehydrogenase (ILDH).

IPA is a ligand of pregnane X receptor (PXR) that regulates TLR4 expression to maintain intestine permeability [16]. Moreover, IPA−PXR regulates vascular endothelial responsiveness by upregulating eNOS [17]. PXR-knockout mice exhibited decreased bone volume resulting from enhanced bone resorption and reduced bone formation [18]. However, the exact role of PXR in osteoclast differentiation remains unclear.

Here, we showed that gut *C. spor.* and its derived metabolite IPA were associated with postmenopausal osteoporosis in mouse models. IPA suppressed osteoclast differentiation by inhibiting RANKL-induced PXR ubiquitination, which led to the degradation of PXR and release of its bound p65. *In vivo* IPA gavage or *C. spor.* transplantation protected against OVX-induced bone loss. A convenient *C. spor.*-encapsulated silk fibroin (SF) hydrogel system achieved bone protection similar to IPA gavage or *C. spor.*

transplantation. Thus, restoring gut *C. spor.* abundance may be a promising strategy for countering postmenopausal osteoporosis.

Methods and Materials

Reagents

IPA was purchased from MedChemExpress (HY-W015229, MedChemExpress, USA). Recombinant M-CSF (#416-ML) and RANKL (#462-TR) were obtained from R&D Systems (Minneapolis, MN, USA). Antibodies against PXR (#ab217375), Ctsk (#ab37259), and TRAP (#ab52750) were purchased from Abcam (Cambridge, UK). Antibodies against Nfatc1 (#8032), c-Fos (#2250), p38 (#8690), JNK (#9252), ERK (#4695), p65 (#8242), NF-κB inhibitor α (IkBa) (#4812), p-p38 (#4511), p-JNK (#9255), p-ERK (#4370), p-p65 (#3033), and p-IkBa (#2859) were obtained from Cell Signaling Technology (MA, USA). MG132 was purchased from MedChemExpress (HY-W015229, MedChemExpress, USA).

BMM isolation and in vitro osteoclast differentiation assay

As previously reported, BMMs were flushed out from the medullary space of the tibia and femur of 8-week-old C57BL/6J mice and then cultured in αMEM medium with 30 ng/mL recombinant M-CSF and 10% fetal bovine serum (FBS) [19]. After 12–16 h, the suspended cells were collected and cultured for 3 days. The adherent cells were then dissociated with 0.25% trypsin for further use. For the osteoclast differentiation assay, 20,000 cells were seeded on 96-well plates and cultured in 200 μL αMEM medium containing 30 ng/mL M-CSF, 75 ng/mL RANKL, and 10% FBS with daily media changes for 5 days.

TRAP staining, F-actin ring formation analysis, and pit formation assay

A TRAP staining kit (387A-1KT, Sigma) was used to visualize osteoclasts after differentiation, according to the manufacturer's instructions. Briefly, the cells were fixed with 4% paraformaldehyde (PFA) for 10 mins and then the staining solution was added. After incubating at 37°C for 1 h, the whole plates were scanned using a microscope (Leica, Munich, Germany), and TRAP-positive multinucleated cells with three or more nuclei were counted as osteoclasts [20].

For the F-actin ring formation assay, BMMs were cultured on the surface of 0.2% collagen gel-coated 6-well plates in the presence of 30 ng/mL M-CSF and 75 ng/mL RANKL for 6 days to induce osteoclast differentiation. Then, the cells were digested with collagenase (0.2%) and seeded onto hydroxyapatite-coated Osteo Assay strip well plates (#3988, Corning, Inc., USA). Thereafter, osteoclasts were treated with various concentrations of IPA for 2 days, and 4% PFA and 0.1% Triton X-100 were used to fix and permeabilize the cells, respectively. Cells were stained with rhodamine-conjugated phalloidin in 2% bovine serum albumin for 1 h. Nuclei were visualized by DAPI staining for 5 min. Images of three fields were randomly captured using a fluorescence microscope (Leica, Munich, Germany). Three patterns of

podosome structures, podosome clusters, actin rings, and podosome belts were counted. ImageJ software was used to quantify the size of F-actin rings.

For pit formation assays, the cells were treated as described in the F-actin ring formation assay and then lysed and washed to expose the bottom from the surface using the 10% bleaching solution, and the resorption pits were captured under a light microscope (Leica, Munich, Germany). The resorption area was analyzed using the ImageJ software (National Institutes of Health).

RT-qPCR

Total mRNA was extracted from cultured cells using the TRIzol reagent (Takara, Japan) according to the manufacturer's protocol. mRNA was reverse-transcribed into cDNA using the HiScript III All-in-one RT SuperMix (Vazyme Biotech Co. Ltd., Nanjing, China), and real-time PCR analyses were performed using the CFX Connect Real-Time System with HiScript II Q RT SuperMix (Vazyme Biotech Co., Ltd., Nanjing, China). The mRNA levels of the target genes were normalized to those of the housekeeping gene β-actin.

WB assay

After washing twice with phosphate buffered saline (PBS), radioimmunoprecipitation assay (RIPA) buffer containing phosphotransferase inhibitor (1%) and proteinase inhibitor (1%) was used to lyse cultured cells. Proteins (20 μg) were separated by 10% SDS-PAGE and transferred to a polyvinylidene difluoride (PVDF) membrane. The membranes were incubated at 4°C overnight with the indicated primary antibodies. Horseradish peroxidase-conjugated anti-mouse or anti-rabbit IgG (5873S, CST) was used as a secondary antibody. Chemiluminescence (#34095; Thermo Fisher Scientific, USA) was used to develop signals, which were quantified via densitometry using Quantity One Software (Bio-Rad Laboratories, USA).

Co-IP assay

For the co-IP assay, two million cells were seeded on 6-cm dishes. The cells were treated with the proteasome inhibitor MG132 (0.5 M) for 10 h before collection. After treatment, the cells were harvested and lysed with specific IP lysis buffer (#P0013, Beyotime, China) containing phosphotransferase inhibitor (1%) and proteinase inhibitor (1%) on ice for 30 min, followed by centrifugation for 5 min at 12,000 rpm at 4°C. The collected lysates were precleared using protein A/G magnetic beads (EngiBody Biotechnology, Shanghai, China). Subsequently, antibodies against the target proteins were mixed with the lysate and incubated at 4°C for 16 h. After four washes with PBS, the co-IP products were collected using protein A/G magnetic beads and analyzed by WB.

IPA measurement

Ten-week-old female C57BL/6J mice were divided into SHAM and OVX groups. Eight weeks after ovariectomy, all mice were sacrificed, and serum was collected. Serum IPA levels were analyzed using an enzyme-linked immunosorbent assay kit (#CB11098-Mu, COIBO BIO, China) following the manufacturer's instructions.

RNA sequencing and analysis

BMMs were divided into IPA-treated and control groups, with four replicates in each group. Total RNA was extracted using an RNAeasy Kit (Qiagen, Germany) according to the manufacturer's guidelines. A total amount of 5 μg of RNA per sample was used as input material for the RNA sample preparations, with mRNA purified from total RNA using poly-T oligo-attached magnetic beads. Following the manufacturer's recommendations (Novogene Co., LTD, China), sequencing libraries were constructed using the NEBNext® UltraTM RNA Library Prep Kit for Illumina® (NEB, USA). Sequencing reads were aligned to the mouse reference genome mm10 (GRCm38.90) using the STAR aligner (v2.5.1b) guided by the mouse GENCODE gene model release v15. HTSeqv0.6.0 was used to count the read numbers mapped to each gene. The fragments per kilobase of transcript per million mapped reads (FPKM) of each gene were calculated based on the length of the gene and the read count mapped to the gene. Raw count data were normalized using the voom function in the R limma package and differential expression analysis was performed using the limma package. DEGs were defined as having at least a 1-fold change in expression and adjusted $P < 0.05$ in comparisons of different genotypes.

Lentivirus transfection

Three short hairpin RNAs (shRNAs) against PXR and a scrambled control lentivirus were purchased from ViGene Biosciences, Inc. The sequences of the shRNAs were as follows: shRNA1, 5'-GGGCCTTGATCAAGAGGAAGATTCAAGAGATCTTCCTCTTGATCAAGGCCCTTTTTT-3,' shRNA2, 5'-GCTACCACTTCAATGTCATTTCAAGAGAATGACATTGAAGTGGTAGCTTTTTT-3,' shRNA3, 5'-GCACAACTTTCTCCCACTTCAATTCAAGAGATTGAAGTGGGAGAAAGTTGTGTTTTTT-3.'

The PXR-overexpressing lentivirus was constructed by Shanghai GeneChem Co. Ltd. (Shanghai, China). The sequence of PXR was obtained from NCBI (All Resources – Site Guide – NCBI; https://www.nih.gov/) and subcloned into a lentivirus vector to overexpress PXR (Over-PXR); the green fluorescent protein (GFP) vector was used as a negative control. The primers used to obtain target DNA fragments and identify recombinant DNA clones are listed in Supplementary Table 1. BMMs were incubated with lentivirus in a complete αMEM medium containing 5 μg/mL polybrene (Thermo Fisher) for 24 h. Subsequently, the cells were harvested to determine the knockdown or overexpression efficiency of each shRNA by qPCR and WB.

16S rRNA sequencing

Fecal samples were processed by Shanghai Majorbio Bio-Pharm Technology Co., Ltd. (Shanghai, China). Total bacterial DNA from the feces was extracted, amplified, and sequenced according to standard procedures. Briefly, microbial DNA was extracted using the E.Z.N.A.® Soil DNA Kit (Omega Bio-tek, Norcross, GA, U.S.) according to the manufacturer's protocol. DNA concentration was assessed using a Nanodrop spectrophotometer (Thermo Scientific, USA) and quality was determined by agarose gel electrophoresis. Bacterial 16S rRNA gene sequences spanning the variable regions V4-V5 were amplified using primers 338F and 806R. The amplicons were then extracted from 2% agarose gels and further

purified using the AxyPrep DNA Gel Extraction Kit (Axygen Biosciences, CA, U.S.) and quantified by QuantiFluor™-ST (Promega, U.S.). Purified amplicons were pooled in equimolar amounts and subjected to paired-end sequencing (2 × 300 bp) on an Illumina MiSeq platform.

Raw FASTQ files were de-multiplexed using an in-house Perl script, and then quality-filtered by fastp version 0.19.6 and merged by FLASH version 1.2.7, with the following criteria: (i) the 300 bp reads were truncated at any site receiving an average quality score of < 20 over a 50 bp sliding window, and the truncated reads shorter than 50 bp were discarded; reads containing ambiguous characters were also discarded; (ii) only overlapping sequences longer than 10 bp were assembled according to their overlapping sequence. The maximum mismatch ratio in the overlapping region was 0.2. Reads that could not be assembled were discarded; (iii) Samples were distinguished according to the barcode and primers, and the sequence direction was adjusted, exact barcode matching, and two nucleotide mismatches in primer matching. Then the optimized sequences were clustered into OTUs using UPARSE 7.1 with a 97% sequence similarity level. The most abundant sequence of each OTU was selected as the representative sequence. To minimize the effects of sequencing depth on alpha and beta diversity measures, the number of 16S rRNA gene sequences from each sample was rarefied to 20,000, which still yielded an average Good's coverage of 99.09%, respectively.

TaqMan real-time PCR

Specific TaqMan real-time PCR for *C. spor.* was performed according to the manufacturer's instructions. A broad-range real-time PCR PP-BioMole-083 assay was used as recommended by the manufacturer. The specific primers used are listed in **Supplementary Table 2**. Thermal cycling was performed using the ABI PRISM 7500 detection system (Applied Biosystems, USA) as follows: 2 min at 50°C for the uracil-N-glycosylase reaction, 2 min at 95°C for denaturation, followed by 10 cycles of 15 s at 95°C, 30 s at 55°C, and 30 s at 72°C, followed by 35 cycles of 15 s at 95°C and 1 min at 60°C.

Fabrication and characterization of bacteria-encapsulated SF hydrogel

SF was prepared using a typical dissolution method. First, the degumming process of silkworm cocoons was operated in an Na_2CO_3 aqueous solution (0.5%, w/v) boiled three times for 20 min each time. The boiled products were rinsed thoroughly with deionized (DI) water until the degummed sericin was completely removed. Then, the degummed SF was fully dried at 40°C for 24 h, and the dried raw SF was dissolved in Ajisawa's reagent, composed of $CaCl_2$: ethanol: H_2O (1:2:8 in molar ratio), for 2 h at 90°C. The dissolved SF solution was centrifuged at 8000 rpm for 20 min to remove insoluble impurities and aggregates. The collected SF solution was dialyzed against DI water for at least three days (MWCO = 3,000 Da). The final SF solution was lyophilized and stored at 4°C.

Bacteria were cultured overnight and suspended at a ratio of 1:100 in liquid culture medium. SF solution (5%, w/v) was prepared and completely mixed with the above liquid at a volume ratio of 10:1. Next, the

mixed solution was sonicated for 30 s at 10% energy power, yielding the injectable **B@SF hydrogel**. Pristine **SF hydrogel** was fabricated as a control.

The morphology and distribution of bacteria in the hydrogels were observed using SEM, JEOL JSM-6510LV, Tokyo, Japan). The viscoelastic behavior of the hydrogel was measured using the Discovery HR-20 Rheometer (AR2000, TA Instruments, USA). The examinations were operated in a parallel-plate model (25-mm diameter) with a 1-mm gap at 37°C. For the time sweep test, the strain and frequency were fixed at 1% and 1 rad/s, respectively. As for the strain sweep test, the frequency was fixed at 1 rad/s, and the stress ranged from 0.1–1000%. For the frequency sweep test, the strain was fixed at 1%, and the frequency ranged from 0.1 to 100 rad/s.

The biodistribution of hydrogels in the GIT was estimated. Firstly, Cy5.5-conjugated SF was prepared using a chemical coupling method and used for hydrogel fabrication. The grafted Cy5.5-SF hydrogel was administered to mice by oral gavage. At different time points after oral gavage (2, 6, 12, and 24 h), the mice were euthanized, and the whole GIT was excised. GIT fluorescence imaging was performed using the Kodak In-Vivo FX Professional Imaging System (CT, USA) to detect the biodistribution of hydrogel in the GIT.

Mouse model of ovariectomy (OVX) and in vivo treatment

Animal experiments were performed according to the principles of the Ethics Committee of Tongji Hospital, Huazhong University of Science and Technology, for the care and use of experimental animals. Eight-week-old C57BL/6J female mice weighing 20 ± 2 g were randomly divided into five groups of six mice each: SHAM + VEHICLE (corn oil); OVX + VEHICLE; OVX + IPA (50 mg/kg body weight); OVX + *C. spor.* (0.26 g/kg tryptophan); and OVX + *C. spor.* + tryptophan diet (2.6 g/kg tryptophan). As reported previously, the OVX model was constructed by removing both ovaries using a dorsal approach. For mice in the SHAM group, the incision was sutured directly after ovarian exposure. One week after surgery, the mice were intragastrically administered IPA or vehicle 7 days a week for 6 weeks. For *C. spor.* re-colonization, as previously reported for *C. spor.* (ATCC15579), the bacteria were cultured anaerobically overnight in trypticase yeast extract medium. The bacterial cultures were mixed with glycerol in hermetically sealed glass vials to obtain a final concentration of 10×10^6 CFU/mL for *C. spor.* *C. spor.* were transplanted into the cecum by oral gavage for 15 consecutive days at a density of 1×10^6 CFU per day.

µCT and histomorphometric analysis

µCT (Scanco Medical, Switzerland) scanning was performed with the parameters of 100 kV, 98 µA, and 10-µm voxel size. Trabecular bone morphometric parametersincluded BV/TV per tissue volume, Tb.N, Tb.Sp, and Tb.Th.

For histomorphometric analysis, femur samples were fixed in 4% PFA for 48 h, followed by decalcification in 15% ethylenediaminetetraacetic acid for 2 weeks and then embedded in paraffin. Subsequently, the

femurs were sectioned into slices (6 μm) for TRAP and H&E staining. TRAP-positive cells with three or more nuclei were quantified using the ImageJ software before calculating Oc.S/BS (%).

Statistical analysis

All data representative of three independent experiments are presented as mean ± SEM. Two-tailed t-tests were conducted to determine the significance between the two groups. One or two-way analysis of variance with Bonferroni post hoc tests was conducted for multiple groups using GraphPad Prism version 5. For all statistical tests, a P-value < 0.05 was considered statistically significant.

Results

C. spor. and its derived IPA are decreased in ovariectomized mice

Ovariectomy mice models were first established to simulate postmenopausal women. As expected, a dramatic decrease in the bone volume to total volume (BV/TV), trabecular number (Tb.N), and trabecular thickness (Tb.Th) was observed in the OVX group compared with the SHAM group (Fig. 1A and Fig. S1A). In contrast, trabecular spacing (Tb.Sp) increased. To determine the changes in gut microbiome induced by ovariectomy, fecal samples were collected for 16S RNA sequencing. Principal component analysis (PCA) explained 22.14% of the total variation in bacterial operational taxonomic units (OTUs), including 13.8% of principal component 1 (PC1) and 8.34% of principal component 2 (PC2), respectively. At the same time, distinct separation along PC1 and PC2 was observed between samples from the OVX and SHAM mice (Fig. 1B). Moreover, Welch's t-test calculated for the Shannon index indicated a significant difference, with a P-value of 0.0038 in the OTU level of gut microbiome distribution between OVX and SHAM mice (Fig. 1C). At the class level, heatmap analysis of the differential flora in both groups revealed that the most abundant bacterial genera were *Bacilli*, *Clostridia*, and *Bacteroidia*. Interestingly, the abundance of *Bacilli* was increased in OVX mice (Fig. 1D-E). In contrast, the abundance of *Clostridia* was decreased, consistent with the results of a previous study conducted in humans [5]. The Wilcoxon rank-sum test bar plot at the class level also confirmed that the abundance of *Clostridia* was significantly decreased in OVX mice. *C. spor.* metabolizes tryptophan to IPA in the gut. Real-time PCR was conducted to determine the abundance of *C. spor.*, which revealed that the abundance of *C. spor.* was decreased in the OVX group (Fig. 1F). Meanwhile, compared with OVX mice, serum concentrations of IPA of SHAM mice were reduced by nearly 80% (Fig. 1G). Taken together, these findings revealed that ovariectomy was associated with decreased abundance of *C. spor.* in the gut and also downregulates serum IPA.

IPA inhibits osteoclast differentiation and bone resorption

To determine the role of IPA in osteoclast formation, osteoclast differentiation assays were performed with and without IPA treatment. Tartrate-resistant acid phosphatase (TRAP) staining results suggested that TRAP-positive cells with multiple nuclei or osteoclasts formed well in the control group after stimulation with M-CSF and RANKL. In contrast, few osteoclasts were observed in the 12.5 μM IPA treatment group; the changes were more obvious in the 25 μM IPA treatment group. In the 50 μM IPA

group, the osteoclast suppression effect was further enhanced (Fig. 2A-B). Consistent with the osteoclast differentiation assays, actin ring formation, as visualized by phalloidin staining, was also inhibited by IPA treatment in a concentration-dependent manner (Fig. 2C). The quantified podosome counts based on phalloidin staining exhibited a significant decrease from 0 μM to 50 μM IPA treatment (Fig. 2D). IPA treatment did not affect bone marrow-derived macrophage (BMM) proliferation, which excluded the possibility that the suppressive effect of IPA on osteoclast differentiation resulted from decreased cell proliferation (Fig. S2). Bone resorption assays showed the resorption area was decreased from 28% in the dimethyl sulfoxide group to 3% in the 50 μM IPA group, which indicated that IPA suppressed osteoclast bone resorption (Fig. 2E-F). Expression levels of osteoclast marker genes and master regulators were also investigated. Molecular analysis by quantitative reverse transcription PCR (RT-qPCR) revealed that the expression of osteoclast markers matrix metallopeptidase 9 (MMP-9), cathepsin K (Ctsk), TRAP, and nuclear factor of activated T cells 1 (Nfatc1) was suppressed in the IPA treatment groups in a concentration-dependent manner (Fig. 2H-K). Western blotting (WB) further revealed decreased protein levels of c-Fos and Nfatc1, two master regulators of osteoclast differentiation, in the IPA-treated groups. The protein levels of other osteoclast markers, such as MMP-9, TRAP, and Ctsk, also decreased (Fig. 2L-P), consistent with the RT-qPCR data. Time-interval incubations revealed that c-Fos was significantly suppressed by IPA after 1-day incubation with RANKL and IPA compared with incubation with RANKL alone. This suppression effect decreased with time. In contrast, the expression of MMP-9, TRAP, and Nfatc1 was obviously decreased after 5 days of incubation with RANKL and IPA (Fig. 2Q-U).

IPA suppresses RANKL-induced NF-κB but not MAPK activation

RNA sequencing was performed to profile transcriptomic changes associated with IPA-induced osteoclast suppression. A total of 448 differentially expressed genes (DEGs) were identified, 366 of which were downregulated by more than two-fold, whereas 82 DEGs were upregulated (Fig. 3A). The Kyoto Encyclopedia of Genes and Genomes analysis of DEGs identified significantly altered pathways such as axon guidance and proteoglycans in cancer. Among these significantly altered pathways, osteoclast differentiation and NF-κB pathways, which are reported to be critical in osteoclast formation [21], attracted our attention (Fig. 3B-D). In the osteoclast differentiation pathway, the expression of Fos, Nfatc1, Ctsk, osteoclast-associated receptor (Oscar), and MMP-9 was obviously decreased in the IPA treatment group, consistent with our previous RT-qPCR data. Meanwhile, TNFRSF11A, TRAF1, MALT1, TNFAIP3, Bcl2a1a, Lat, and CARD14 in NF-κB pathway were downregulated in the IPA treatment group (Fig. 3E). These findings indicated that the NF-κB pathway might participate in IPA-induced changes in osteoclast differentiation.

NF-κB and MAPK are two critical pathways activated by RANKL/RANK interaction [21]. To assess potential changes in the activation of NF-κB and MAPK pathways induced by IPA, cells were starved in serum-free media and pretreated with IPA for 16 h, followed by RANKL treatment for the indicated time intervals. As expected, phosphorylation of p65 by IκBα was dramatically increased after 15 min of incubation with RANKL. However, as shown by quantified p-p65 to total p65 and p-IκBα to total IκBα data, RANKL-induced

changes were decreased by IPA treatment (Fig. 3F-G). In contrast, IPA pretreatment did not change the RANKL-induced p-p38, p-ERK, or p-JNK (Fig. 3H-I). The data demonstrated that NF-κB, but not MAPK, was involved in IPA treatment-induced osteoclast suppression.

IPA suppresses osteoclast differentiation by activating PXR

PXR is a receptor of IPA [22,23]. To determine the potential role of PXR in IPA-induced osteoclast suppression, RT-qPCR for genes downstream of PXR, including *CYP3a11*, *MDR1*, and *UGT1a1*, was performed. All three genes were upregulated by IPA treatment (Fig. S3A), indicating that PXR was activated by IPA. To determine the function of PXR in osteoclast differentiation, we first evaluated changes in PXR expression during osteoclast formation. PXR expression decreased from day 0 to day 1 during osteoclast differentiation at both the mRNA and protein levels and remained low thereafter (Fig. 4A-B). To further assess whether the inhibition of osteoclasts by IPA occurred by activating PXR, we constructed an shRNA targeting PXR (sh-PXR). The knockdown efficiency of sh-PXR was assessed using RT-qPCR and WB analysis (Fig. S3B-C). TRAP staining suggested that the inhibitory effect of IPA on osteoclast differentiation was abrogated by PXR silencing (Fig. 4C-D). Similarly, F-actin ring formation was restored by sh-PXR (Fig. 4E-F). In addition, IPA-induced inhibition of osteoclast resorption was eliminated (Fig. 4G-H). Further biochemical assays confirmed that sh-PXR rescued the IPA-induced downregulation of osteoclast markers, including Nfatc1, MMP-9, c-Fos, and TRAP, at both the mRNA (Fig. 4I-L) and protein (Fig. 4M-R) levels. Thus, IPA inhibits osteoclast differentiation and function by activating PXR.

IPA inhibits the release of p65 from PXR by suppressing PXR ubiquitination

To elucidate the function of PXR in osteoclast differentiation, we constructed a PXR-overexpressing plasmid (over-PXR) (Fig. S4A). PXR overexpression directly inhibited osteoclast differentiation and suppressed F-actin ring formation (Fig. 5A-D). In addition, PXR overexpression significantly inhibited bone resorption by osteoclasts (Fig. 5E-F). Further, RT-qPCR and WB experiments showed that PXR overexpression suppressed the expression of RANKL-induced osteoclast markers (Fig. 5G-K). Meanwhile, RANKL-induced NF-κB activation was suppressed by IPA treatment, as indicated by decreased phosphorylation of p65 and IκBα at 15 and 30 min after RANKL incubation (Fig. 5L and Fig. S4B-D).

Our previous results revealed a significant decrease in PXR expression after 1 day of incubation with RANKL, and it remained at a low level, raising the question of whether changes in PXR expression upon RANKL stimulation were initiated earlier. A short time-point assay demonstrated that PXR was downregulated as soon as 15 min/30 min/1 h after RANKL incubation. However, IPA treatment blocked this process, indicating a potential post-translational modification mechanism (Fig. 5M). Human PXR can be ubiquitinated, leading to proteasome-related degradation, which suggests that ubiquitination is responsible for RANKL-induced PXR decrease at the protein level [24]. To investigate this, PXR was pulled down, followed by WB analysis for ubiquitination. The data suggested that RANKL treatment increased the ubiquitination of PXR, whereas IPA treatment attenuated this change (Fig. 5P). Furthermore, it has

been shown that NF-κB p65 disrupts the association of the PXR-RXRα complex by interacting with the DNA-binding domain of RXRα [25]. Therefore, we investigated whether PXR interacted with p65. Co-immunoprecipitation (co-IP) assays showed that PXR directly bound to p65, which is different from previous findings for the PXR.RXRα complex [25]. We also found that RANKL treatment decreased PXR-bound p65 (Fig. 5Q). In contrast, IPA treatment restored the binding of PXR with p65. Moreover, immunofluorescence experiments showed that RANKL stimulation decreased PXR expression and reduced the overlap of p65 with PXR (Fig. 5R). IPA treatment restored PXR expression and promoted its overlapping with p65. These findings demonstrate that IPA activates PXR, leading to increased PXR ubiquitination. PXR degradation results in p65 release, which contributes to osteoclast differentiation.

Both IPA supplementation and C. spor. colonization protect mice against OVX-induced bone loss

Our *in vitro* experiments revealed that IPA suppressed osteoclast formation and function. OVX treatment led to a significant reduction in the abundance of *C. spor.* in the gut and its derived IPA in the serum, prompting us to investigate the *in vivo* effects of *C. spor.* IPA supplementation on OVX-induced osteoporosis. To address this question, mice were randomly divided into five groups. The OVX mice were treated with vehicle (corn oil) or IPA (50 mg/kg body weight) daily via oral gavage for 60 days. The other OVX mice were administered *C. spor.* colonization with or without tryptophan supplementation.

Serum IPA levels confirmed that *C. spor.* colonization was effectively upregulated IPA in circulation, and additional tryptophan supplementation further enhanced it (Fig. 6B). Microcomputed tomography (μCT) scanning suggested a dramatic decrease in the trabecular bone fraction (BV/TV) in OVX mice treated with the vehicle compared with that in SHAM mice (Fig. 6C). The decrease in bone mass resulted from decreased Tb.N and Tb.Th and increased Tb.Sp (Fig. 6C). Importantly, OVX mice treated with IPA exhibited a significant increase in BV/TV compared with OVX mice treated with vehicle (Fig. 6C-G), indicating that IPA treatment protected OVX mice from bone loss. Interestingly, BV/TV of the *C. spor.* colonization group was higher than that of the SHAM group but not as effective as that with IPA treatment. Tryptophan supplementation in diet resulted in an additional increase in bone volume in conjunction with *C. spor.* colonization, compared with *C. spor.* colonization alone, which could be explained by increased IPA in the serum (Fig. 6B).

Furthermore, TRAP and H&E staining of the bone sections indicated an increased osteoclast surface/bone surface ratio (Oc.S/BS) in mice in the OVX + VEH group compared with that in mice in the SHAM + VEH group. However, Oc.S/BS decreased following IPA treatment and *C. spor.* colonization (Fig. 6H-J). Moreover, the combination of *C. spor.* colonization and tryptophan supplementation provided better protection against OVX-induced osteoclast increases than *C. spor.* colonization alone. In summary, both IPA treatment and *C. spor.* colonization, in combination with tryptophan supplementation, prevent ovariectomy-induced bone loss by suppressing osteoclast formation.

C. spor. encapsulated SF hydrogel treatment inhibits OVX-induced bone loss

C. spor. colonization in combination with tryptophan supplementation in diet significantly protected against OVX-induced bone loss. However, the disadvantages of direct oral bacterial administration may prevent its translational use. First, live bacteria have to survive in the gastric fluid before colonizing the gut, which may disrupt stomach homeostasis. In addition, the relatively short gastrointestinal transit time in mice (approximately 8 h) [26] may limit sufficient *C. spor* colonization. To overcome these limitations, we developed an encapsulated SF hydrogel system for *C. spor.* delivery. The SF hydrogel was prepared via ultrasonic induction through the formation of a β-sheet structure and hydrogen bonds between intra- and intermolecular SF polymer chains.

SEM images showed that the SF hydrogel possessed a honeycomb-like porous microstructure (Fig. 7A). Enlarged images of the bacteria-encapsulated SF hydrogel (B@SF hydrogel) demonstrated even distribution of bacteria within the hydrogel network (Fig. 7A). The viscoelastic properties of the SF and B@SF hydrogels were investigated using rheological measurements. After sonication, the hydrogel was immediately subjected to a rheological sweep. As shown in Fig. 7B, the hydrogel's storage modulus (G') dramatically increased over time, attributed to the increased β-sheet crosslinking formation inside the hydrogel. Furthermore, the results of the time (Fig. 7B), frequency (Fig. 7C), and strain sweeps (Fig. 7D) showed no significant difference between the SF and B@SF hydrogel groups, demonstrating that bacterial encapsulation had no negative effect on hydrogel formation. To observe the distribution of the SF hydrogel in the gastrointestinal tract (GIT), an *in vivo* fluorescence imaging system was used. The imaging results showed that the fluorescence gradually moved from the anterior to the posterior GIT over time, and finally, the cecum and colorectum exhibited the strongest fluorescence intensity at 12 h (Fig. 7E). These results suggested that the B@SF hydrogel was effectively retained in the GIT and concentrated in the colorectal area in accordance with the peristaltic rhythm of the GIT. After 24 h of gavage, the fluorescence in the GIT showed a relatively low intensity, suggesting that the hydrogel was expelled from the body. These data suggest that the SF hydrogel is a suitable oral carrier for delivering bacteria to the GIT and prolonging their retention time in the GIT. Further *in vivo* experiments showed that B@SF hydrogel administration five times at 3-day intervals significantly increased serum IPA levels. When the B@SF hydrogel was administered with tryptophan supplementation, this effect was further enhanced. μCT scanning demonstrated that B@SF hydrogel administration alone partially prevented OVX-induced bone loss (Fig. 7H-L). Meanwhile, B@SF hydrogel administration with a tryptophan diet achieved comparable protection against OVX-induced bone loss to daily IPA supplementation, as revealed by increased BV/TV and Tb.N and decreased Tb.Sp. Furthermore, H&E and TRAP staining of the bone sections indicated Oc.S/BS (%) (Fig. 7M-O). Overall, *C. spor.*-encapsulated SF hydrogel treatment is a convenient and effective method for combating OVX-induced bone loss.

Discussion

In this study, we investigated the contribution of gut microbiome to the pathogenesis of postmenopausal osteoporosis in a mouse model. The results identified *C. spor.*, as well as its derived metabolite IPA, to be decreased in OVX mice. IPA was found to suppress osteoclast differentiation *in vitro* by activating PXR,

which led to p65 release through ubiquitination. Administering *C. spor.* in combination with a tryptophan diet provided similar protection against OVX-induced bone loss as direct IPA administration. To minimize repeated drug or microbiota administration, we developed the *C. spor.*-encapsulated SF hydrogel system, which offered comparable protection against OVX-induced bone loss with fewer total treatment times compared with direct *C. spor.* colonization.

The role of gut microbiome in regulating bone homeostasis via SCFAs has been recognized, but its specific contribution to postmenopausal osteoporosis remains unclear. Our 16S RNA sequencing results indicated significant differences in *Bacilli* and *Clostridia* between the SHAM and OVX groups. As one of the most abundant bacteria in the human and animal intestines, *Clostridium* spp. is mainly composed of clusters IV and XIVa. Cluster IV includes four members: *C. leptum, C. sporosphaeroides, C. cellulosi, and Faecalibacterium prausnitzii.* Although our study focused on *C. spor.*, we cannot exclude the potential contribution of other components in Cluster IV or bacteria in Cluster XIVa to postmenopausal osteoporosis. Additionally, *Bacilli* have been reported to affect bone homeostasis [27] [28].

IPA generated from tryptophan by *C. spor.* has been revealed to be involved in various diseases [29] [30]. Several other bacteria, such as *C. cadaveris, C. botulinum*, and *Peptostreptococcus anaerobius*, have also been shown to produce IPA from tryptophan [31]. However, the relative contributions of different bacteria to IPA in circulation remain unknown. IPA activates both PXR and AhR [16] [22]. While PXR suppresses osteoclast formation, AhR promotes osteoclast differentiation and function by activating c-Fos and NF-κB signaling [32]. Thus, targeting both PXR activation and AhR inhibition may lead to a more significant decrease in osteoclast differentiation.

PXR has emerged as a promising target in energy homeostasis, immune responses, and cancer [33]. Several PXR agonists have been identified in humans and rodents, including hyperforin, rifampicin, forskolin, artemisinin, schisandrol B, and paclitaxel [34]. Specifically, a phase 4 clinical trial was conducted to evaluate the effects of rifampicin on glucose, lipid, and hormone homeostasis. Although subsequent data from the study by Hukannen et al. did not show much benefit of rifampicin on lipid metabolism, glucose tolerance, or hypertension [35] [36] [37], it promoted bone formation, as revealed by increased ALP [38]. These results indicate that PXR is a safe treatment target in humans and may be promising for combating bone diseases.

Microbiota transplantation has been used clinically to treat recurrent *C. difficile* infections. However, the delivery routes for microbiota transplantation are associated with adverse events, with transplantation via the upper GIT having higher incidence rates of adverse events (43.9%) than that via the lower gastrointestinal tract (20.6%) [39]. After oral administration, the microbiota pass through the GIT from the mouth and stomach to the small intestine and colon. In the stomach, the microbiota are exposed to acidic gastric fluid, which is lethal to most bacteria. In addition, the viability of transplanted microbiota is affected by ionic strength, pepsin activity, and mechanical churning [40]. Methods such as enteric coating and enteric microencapsulated formulations have been developed to protect probiotics against the harsh

environment in the stomach and help probiotic bacteria colonize the intestine or colon [41]. The SF hydrogel system reported here delays gastrointestinal transit time, allowing for colonization of more bacteria in the gut and improved survival of loaded bacteria in the harsh stomach environment.

In conclusion, this study identified that *C. spor.* in the gut and its derived IPA were decreased in OVX mice. Administration of the *C. spor.*-encapsulated SF hydrogel system protected OVX mice from bone loss, thus offering a promising treatment method for postmenopausal osteoporosis.

Declarations

All the animal study in the manuscript "Gut Clostridium sporogenes-derived indole propionic acid suppresses osteoclast formation by activating pregnane X receptor" was approved by the Ethics Committee of Tongji Hospital, Huazhong University of Science and Technology.

Acknowledgments

Conflict of interests

The authors declare no conflicts of interests.

Author contributions

LF and PRP conceived of and designed the study. PRP and SC performed most of the experiments, analyzed the data, and wrote the manuscript. LF, GHF, and FQ provided guidance and advice during the experimentation and analysis of the results. LHY, KHL, DYM, and XY assisted with animal experiments. GSQ and FQ provided the essential reagents, equipment, and advice. LF and GHF provided feedback on the experiments and reviewed and edited the manuscript. Final approval of the manuscript was obtained from all the authors. All authors contributed to the manuscript and approved the submitted version.

References

1. Duran, A. *et al.* The atypical PKC-interacting protein p62 is an important mediator of RANK-activated osteoclastogenesis. Dev Cell 6, 303–309 (2004). https://doi.org:10.1016/s1534-5807(03)00403-9

2. Mizukami, J. *et al.* Receptor activator of NF-kappaB ligand (RANKL) activates TAK1 mitogen-activated protein kinase kinase kinase through a signaling complex containing RANK, TAB2, and TRAF6. Mol Cell Biol 22, 992–1000 (2002). https://doi.org:10.1128/MCB.22.4.992-1000.2002

3. Abu-Amer, Y. NF-kappaB signaling and bone resorption. Osteoporos Int 24, 2377–2386 (2013). https://doi.org:10.1007/s00198-013-2313-x

4. Lee, K., Seo, I., Choi, M. H. & Jeong, D. Roles of Mitogen-Activated Protein Kinases in Osteoclast Biology. Int J Mol Sci 19 (2018). https://doi.org:10.3390/ijms19103004

5. Rettedal, E. A., Ilesanmi-Oyelere, B. L., Roy, N. C., Coad, J. & Kruger, M. C. The Gut Microbiome Is Altered in Postmenopausal Women With Osteoporosis and Osteopenia. JBMR Plus 5, e10452 (2021). https://doi.org:10.1002/jbm4.10452

6. He, J. *et al.* Gut microbiota and metabolite alterations associated with reduced bone mineral density or bone metabolic indexes in postmenopausal osteoporosis. Aging (Albany NY) 12, 8583–8604 (2020). https://doi.org:10.18632/aging.103168

7. Jansson PA, C. D., Ahren IL, Hansson F, Niskanen TM, Sjogren K, Ohlsson C. Probiotic treatment using a mix of three Lactobacillus strains for lumbar spine bone loss in postmenopausal women: a randomised, double-blind, placebo-controlled, multicentre trial. Lancet Rheumatology 1, E154-162 (2019). https://doi.org:https://doi.org/10.1016/S2665-9913(19)30068-2

8. Sjogren, K. *et al.* The gut microbiota regulates bone mass in mice. Journal of bone and mineral research: the official journal of the American Society for Bone and Mineral Research 27, 1357–1367 (2012). https://doi.org:10.1002/jbmr.1588

9. Yan, J. *et al.* Gut microbiota induce IGF-1 and promote bone formation and growth. Proceedings of the National Academy of Sciences of the United States of America 113, E7554-E7563 (2016). https://doi.org:10.1073/pnas.1607235113

10. Cho, S. W. *et al.* Positive regulation of osteogenesis by bile acid through FXR. Journal of bone and mineral research: the official journal of the American Society for Bone and Mineral Research 28, 2109–2121 (2013). https://doi.org:10.1002/jbmr.1961

11. Go, M., Shin, E., Jang, S. Y., Nam, M., Hwang, G. S. & Lee, S. Y. BCAT1 promotes osteoclast maturation by regulating branched-chain amino acid metabolism. Exp Mol Med 54, 825–833 (2022). https://doi.org:10.1038/s12276-022-00775-3

12. Su, Y., Elshorbagy, A., Turner, C., Refsum, H., Chan, R. & Kwok, T. Circulating amino acids are associated with bone mineral density decline and ten-year major osteoporotic fracture risk in older community-dwelling adults. Bone 129, 115082 (2019). https://doi.org:10.1016/j.bone.2019.115082

13. Wang, N., Hao, Y. & Fu, L. Trimethylamine-N-Oxide Promotes Osteoclast Differentiation and Bone Loss via Activating ROS-Dependent NF-kappaB Signaling Pathway. Nutrients 14 (2022). https://doi.org:10.3390/nu14193955

14. Roager, H. M. & Licht, T. R. Microbial tryptophan catabolites in health and disease. Nat Commun 9, 3294 (2018). https://doi.org:10.1038/s41467-018-05470-4

15. Nagano, Y., Itoh, K. & Honda, K. The induction of Treg cells by gut-indigenous Clostridium. Curr Opin Immunol 24, 392–397 (2012). https://doi.org:10.1016/j.coi.2012.05.007

16. Venkatesh, M. *et al.* Symbiotic bacterial metabolites regulate gastrointestinal barrier function via the xenobiotic sensor PXR and Toll-like receptor 4. Immunity 41, 296–310 (2014).

https://doi.org:10.1016/j.immuni.2014.06.014

17. Pulakazhi Venu, V. K. *et al.* The pregnane X receptor and its microbiota-derived ligand indole 3-propionic acid regulate endothelium-dependent vasodilation. Am J Physiol Endocrinol Metab 317, E350-E361 (2019). https://doi.org:10.1152/ajpendo.00572.2018

18. Azuma, K. *et al.* Pregnane X receptor knockout mice display osteopenia with reduced bone formation and enhanced bone resorption. The Journal of endocrinology 207, 257–263 (2010). https://doi.org:10.1677/JOE-10-0208

19. Shin, B., Kupferman, J., Schmidt, E., Polleux, F., Delany, A. M. & Lee, S. K. Rac1 Inhibition Via Srgap2 Restrains Inflammatory Osteoclastogenesis and Limits the Clastokine, SLIT3. J Bone Miner Res 35, 789–800 (2020). https://doi.org:10.1002/jbmr.3945

20. Guo, Q. *et al.* Inhibition of ACLY Leads to Suppression of Osteoclast Differentiation and Function Via Regulation of Histone Acetylation. J Bone Miner Res (2021). https://doi.org:10.1002/jbmr.4399

21. William J. Boyle, W. S. S., David L. Lacey. Osteoclast differentiation and activation. *nature* 423, 337–342 (2003). https://doi.org:DOI: 10.1038/nature01658

22. Sari, Z. *et al.* Indolepropionic Acid, a Metabolite of the Microbiome, Has Cytostatic Properties in Breast Cancer by Activating AHR and PXR Receptors and Inducing Oxidative Stress. Cancers (Basel) 12 (2020). https://doi.org:10.3390/cancers12092411

23. Xiao, H. W. *et al.* Gut microbiota-derived indole 3-propionic acid protects against radiation toxicity via retaining acyl-CoA-binding protein. Microbiome 8, 69 (2020). https://doi.org:10.1186/s40168-020-00845-6

24. Rana, R., Coulter, S., Kinyamu, H. & Goldstein, J. A. RBCK1, an E3 ubiquitin ligase, interacts with and ubiquinates the human pregnane X receptor. Drug Metab Dispos 41, 398–405 (2013). https://doi.org:10.1124/dmd.112.048728

25. Gu, X. *et al.* Role of NF-kappaB in regulation of PXR-mediated gene expression: a mechanism for the suppression of cytochrome P-450 3A4 by proinflammatory agents. J Biol Chem 281, 17882–17889 (2006). https://doi.org:10.1074/jbc.M601302200

26. Padmanabhan, P., Grosse, J., Asad, A. B., Radda, G. K. & Golay, X. Gastrointestinal transit measurements in mice with 99mTc-DTPA-labeled activated charcoal using NanoSPECT-CT. EJNMMI Res 3, 60 (2013). https://doi.org:10.1186/2191-219X-3-60

27. Chen, C. *et al.* The role of Bacillus acidophilus in osteoporosis and its roles in proliferation and differentiation. J Clin Lab Anal 34, e23471 (2020). https://doi.org:10.1002/jcla.23471

28. Sapra, L. *et al.* Lactobacillus rhamnosus attenuates bone loss and maintains bone health by skewing Treg-Th17 cell balance in Ovx mice. Sci Rep 11, 1807 (2021). https://doi.org:10.1038/s41598-020-80536-2

29. Xue, H. *et al.* Gut Microbially Produced Indole-3-Propionic Acid Inhibits Atherosclerosis by Promoting Reverse Cholesterol Transport and Its Deficiency Is Causally Related to Atherosclerotic Cardiovascular Disease. Circ Res 131, 404–420 (2022). https://doi.org:10.1161/CIRCRESAHA.122.321253

30. Zhao, Z. H. *et al.* Indole-3-propionic acid inhibits gut dysbiosis and endotoxin leakage to attenuate steatohepatitis in rats. Exp Mol Med 51, 1–14 (2019). https://doi.org:10.1038/s12276-019-0304-5

31. Dodd, D. *et al.* A gut bacterial pathway metabolizes aromatic amino acids into nine circulating metabolites. Nature 551, 648–652 (2017). https://doi.org:10.1038/nature24661

32. Izawa, T. *et al.* The Nuclear Receptor AhR Controls Bone Homeostasis by Regulating Osteoclast Differentiation via the RANK/c-Fos Signaling Axis. J Immunol 197, 4639–4650 (2016). https://doi.org:10.4049/jimmunol.1600822

33. Lynch, C., Sakamuru, S., Huang, R., Niebler, J., Ferguson, S. S. & Xia, M. Characterization of human pregnane X receptor activators identified from a screening of the Tox21 compound library. Biochem Pharmacol 184, 114368 (2021). https://doi.org:10.1016/j.bcp.2020.114368

34. Staudinger, J. L., Ding, X. & Lichti, K. Pregnane X receptor and natural products: beyond drug-drug interactions. Expert Opin Drug Metab Toxicol 2, 847–857 (2006). https://doi.org:10.1517/17425255.2.6.847

35. Hassani-Nezhad-Gashti, F. *et al.* Activation of nuclear receptor PXR impairs glucose tolerance and dysregulates GLUT2 expression and subcellular localization in liver. Biochem Pharmacol 148, 253–264 (2018). https://doi.org:10.1016/j.bcp.2018.01.001

36. Hassani-Nezhad-Gashti, F., Salonurmi, T., Hautajarvi, H., Rysa, J., Hakkola, J. & Hukkanen, J. Pregnane X Receptor Activator Rifampin Increases Blood Pressure and Stimulates Plasma Renin Activity. Clin Pharmacol Ther 108, 856–865 (2020). https://doi.org:10.1002/cpt.1871

37. Rahunen, R. *et al.* Pregnane X Receptor4beta-Hydroxycholesterol Axis in the Regulation of Overweight- and Obesity-Induced Hypertension. J Am Heart Assoc 11, e023492 (2022). https://doi.org:10.1161/JAHA.121.023492

38. Nabil, H. *et al.* Rifampicin induces the bone form of alkaline phosphatase in humans. Basic Clin Pharmacol Toxicol 130 Suppl 1, 81–94 (2022). https://doi.org:10.1111/bcpt.13586

39. Bonovas, S., Fiorino, G., Lytras, T., Nikolopoulos, G., Peyrin-Biroulet, L. & Danese, S. Systematic review with meta-analysis: use of 5-aminosalicylates and risk of colorectal neoplasia in patients with inflammatory bowel disease. Aliment Pharmacol Ther 45, 1179–1192 (2017). https://doi.org:10.1111/apt.14023

40. Sarao, L. K. & Arora, M. Probiotics, prebiotics, and microencapsulation: A review. Crit Rev Food Sci Nutr 57, 344–371 (2017). https://doi.org:10.1080/10408398.2014.887055

41. Yus, C. *et al.* Targeted Release of Probiotics from Enteric Microparticulated Formulations. Polymers (Basel) 11 (2019). https://doi.org:10.3390/polym11101668
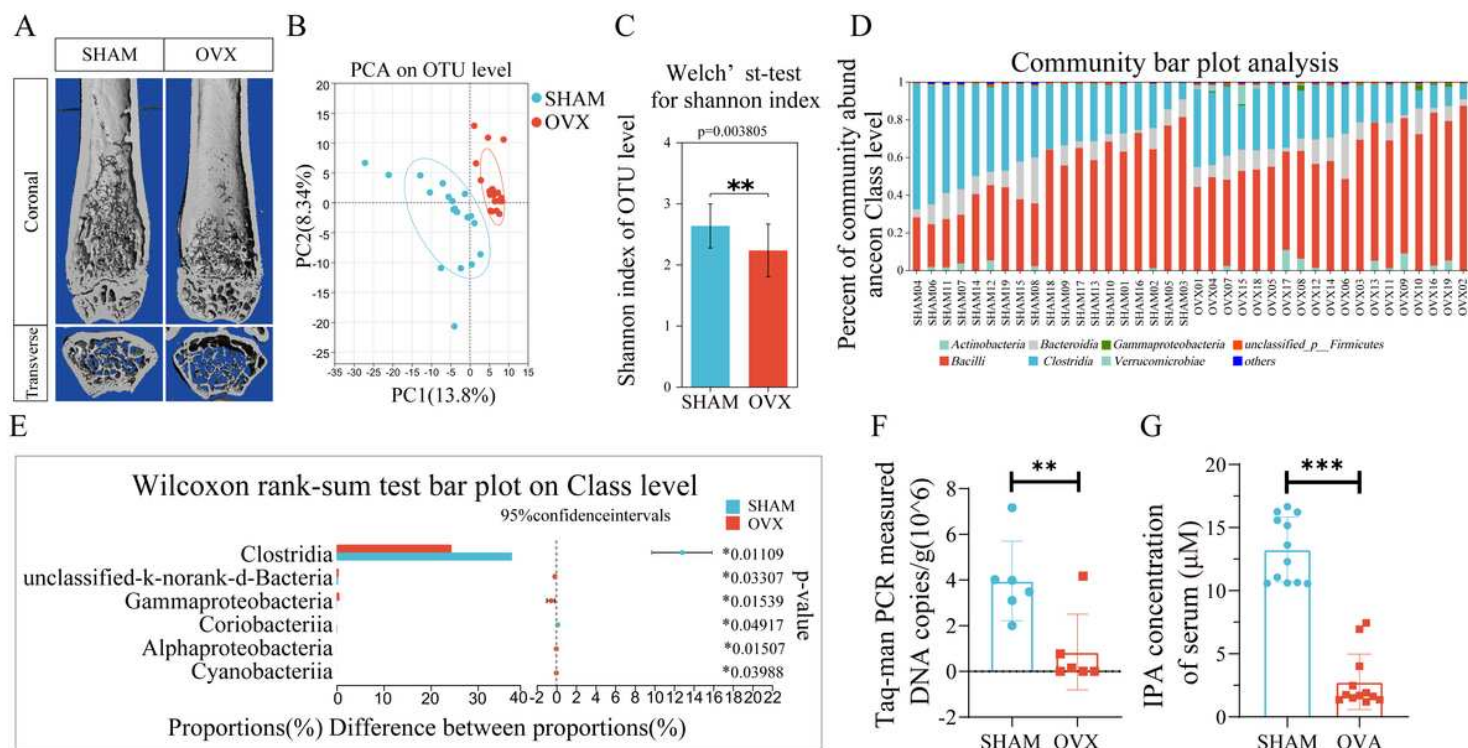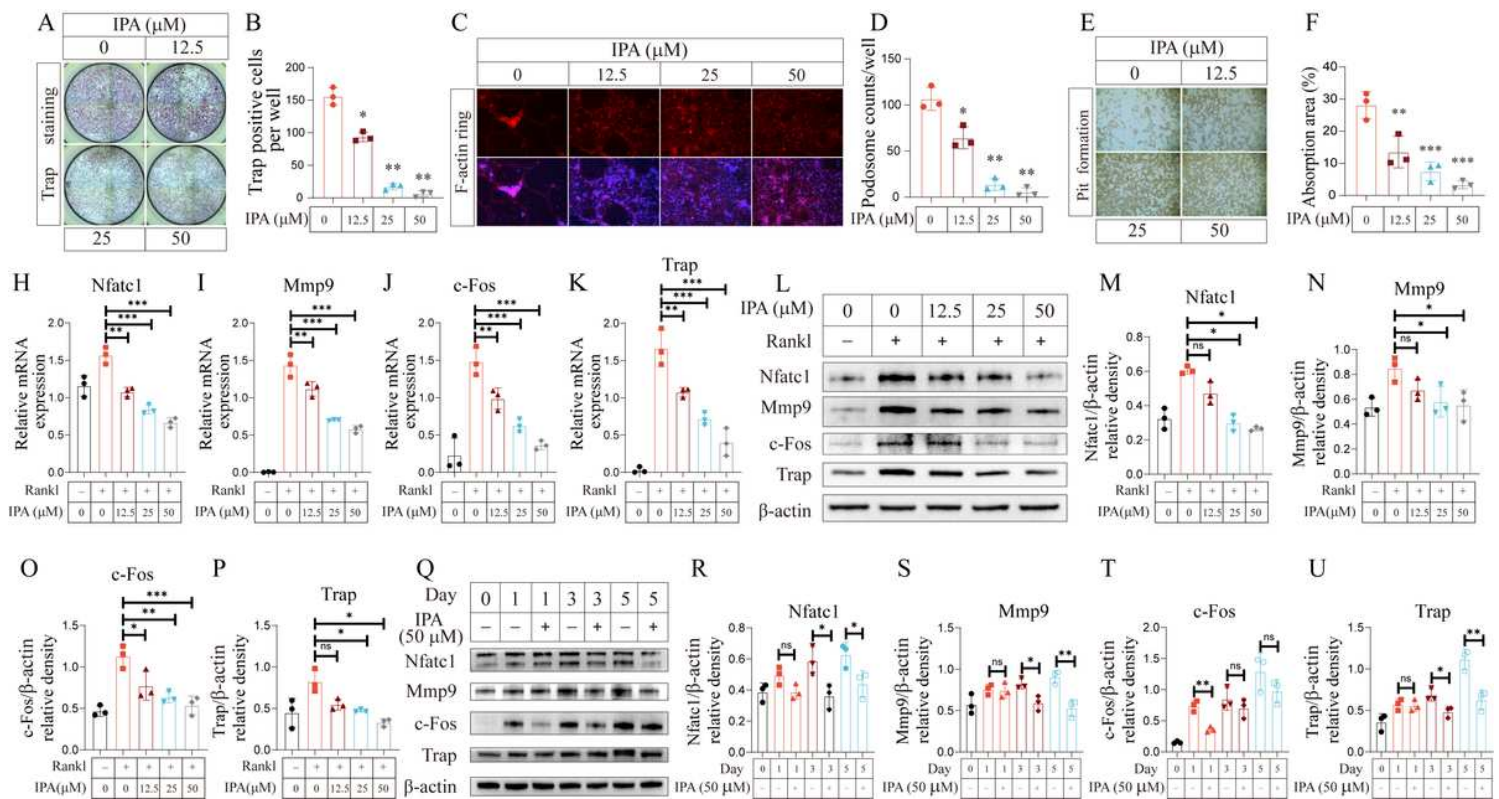
Figures

Figure 1

C. spor. and its derived IPA are decreased in ovariectomized mice

(A) Representative 3D-reconstructed images of the distal femurs of mice from the OVX and SHAM groups. (B) Principal component analysis (PCA) showing differences in the gut microbiome of stool samples from 19 SHAM (SHAM, blue) and 19 OVX (OVX, red) mice. (C) Shannon index of Welch's t-test showing differences in the gut microbiome of stool samples from SHAM (SHAM, blue) and OVX (OVX, red) mice. (D) Comparison of class-level proportional abundance of the gut microbiome in stool samples from SHAM and OVX mice. (E) Wilcoxon rank-sum test identified six gut microbiomes in stool samples at the class level. (F) Taq-man PCR for DNA copied of C. spor. in fecal samples from SHAM and OVX mice. (H) IPA levels in the serum of SHAM mice and OVX mice. Data are shown as mean ± SEM. * P < 0.05, ** P < 0.01, and *** P < 0.001.
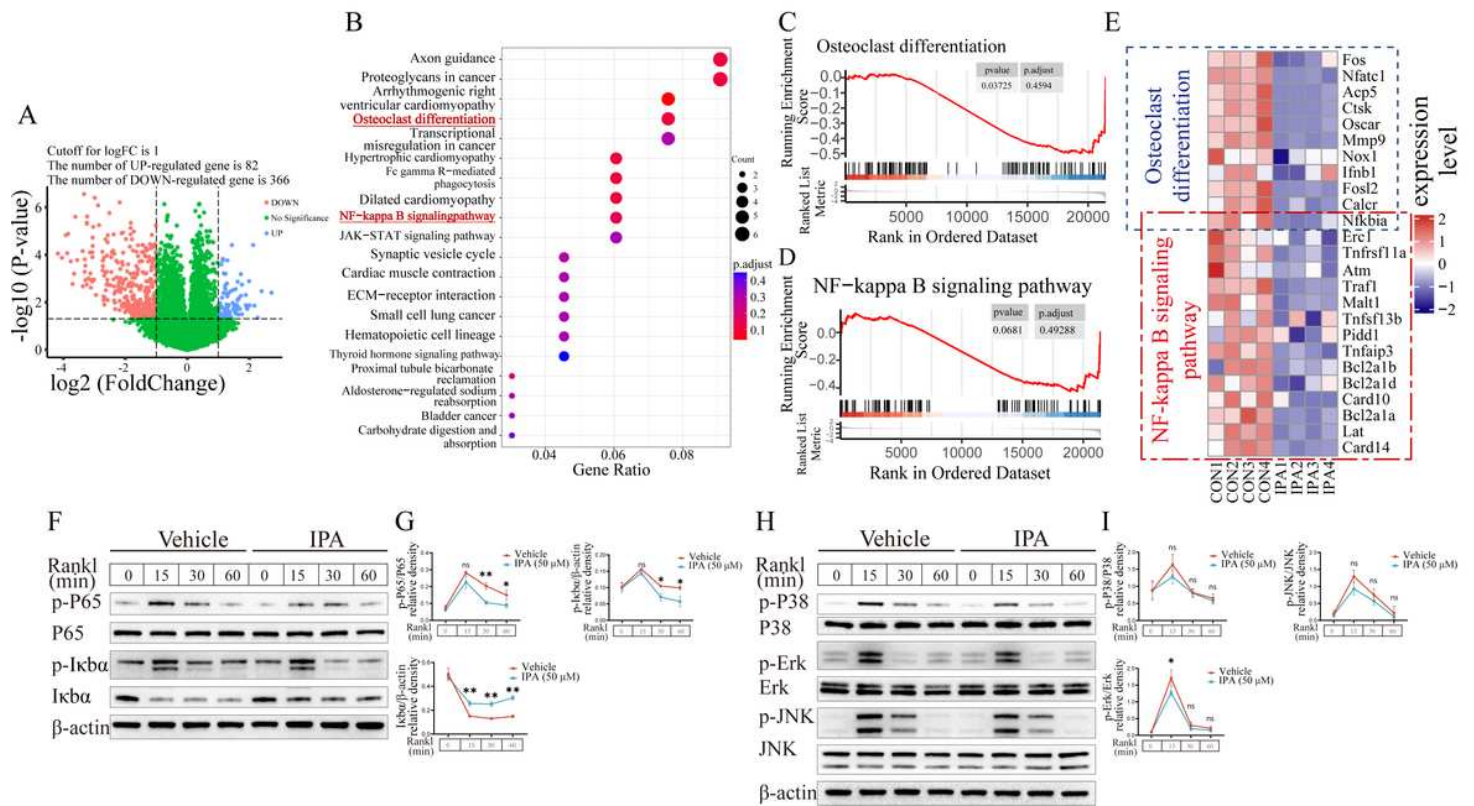
Figure 2

IPA inhibits osteoclast differentiation and bone resorption

(A, B) IPA suppressed RANKL-induced osteoclastogenesis in a concentration-dependent manner. BMMs were treated with different concentrations of IPA (0, 12.5, 25, and 50 μM), with induction by M-CSF and RANKL for 5 days.TRAP-positive multinucleated (> 3 nuclei) cells were counted as osteoclasts. (C, D) BMMs were seeded on 0.2% collagen-gel-coated six-well plates and stimulated with 30 ng/mL M-CSF and 75 ng/mL RANKL for 6 days. Then, the cells were digested and seeded onto the Osteo Assay strip well plates. Mature osteoclasts were treated with various concentrations of IPA for 3 days. F-actin staining was performed, and three patterns of podosome—podosome clusters, actin rings, and podosome belts—were counted. (E, F) Mature osteoclasts were cultured on Osteo Assay strip well plates and treated with the medium containing M-CSF and RANKL in combination with various concentrations of IPA for 3 days. The cells were then washed from the surface by using the 10% bleaching solution for 5 min. Resorption pits were captured with light microscopy and analyzed using Image J software. (H-K) BMMs were cultured with the medium containing M-CSF, RANKL, and IPA of a series of concentrations for 3 days. Relative mRNA expression levels of Nfatc1, MMP-9, c-Fos, and TRAP versus β-actin were quantified using qPCR. (L-P) BMMs were treated with indicated concentrations of IPA (0, 12.5, 25, and 50 μM) with stimulation by M-CSF and RANKL for 3 days, and protein expression of osteoclast-specific genes was determined using Western blot. (Q-U) BMMs were treated with indicated concentrations of IPA (50 μM) with stimulation by M-CSF and RANKL for 0, 1, 3, and 5 days. The protein expression of osteoclast-specific genes was determined using Western blot. *P < 0.05, **P < 0.01 and *** P < 0.001. NS, no significance.
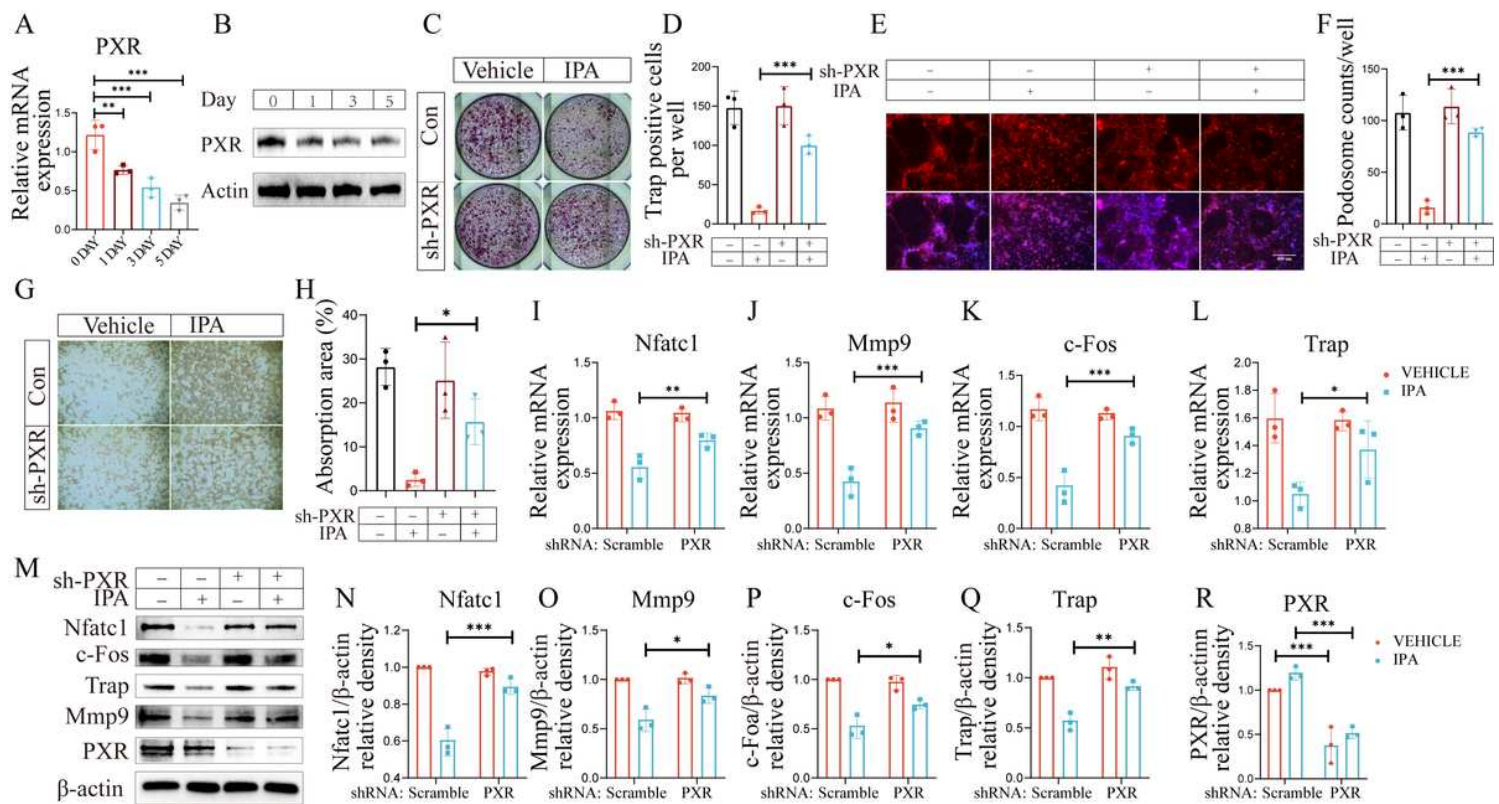
Figure 3

## IPA suppresses RANKL-induced NF-κB but not MAPK activation

(A) Volcano plot showing differentially expressed genes between the control and IPA treatment groups. A total of 82 upregulated and 366 downregulated genes were identified by setting the threshold of log2 (fold change) to 1 and the P-value to 0.05. (B) Kyoto Encyclopedia of Genes and Genomes enrichment analysis showed that the osteoclast differentiation and NF-kappa B signaling pathways were significantly altered after IPA treatment. (C, D) GSEA analysis confirmed the inhibition of the osteoclast differentiation and NF-kappa B signaling pathways by IPA. (E) Heatmaps showed the downregulated genes in the osteoclast differentiation and NF-kappa B signaling pathways. (F-I) Western blot assay detected RANKL-induced phosphorylation of p65 and IκBα of the NF-kappa B signaling pathway and JNK, ERK, and p38 of the MAPK pathway after IPA pretreatment.* P < 0.05; ** P < 0.01; *** P < 0.001; NS, no significance.

Figure 4

IPA suppresses OC differentiation through activating PXR

(A, B) BMMs were treated with RANKL for the indicated times (day 0, 1, 3, and 5). The mRNA and protein expression of PXR were determined using qPCR and Western blot, respectively. (C, D) BMMs were infected with the lentivirus carrying PXR shRNA or the control lentivirus and then cultured in the presence of M-CSF and RANKL for 5 days with or without IPA (50 μM) treatment, followed by TRAP staining. TRAP-positive cells with three or more nuclei were counted as osteoclasts. (E, F) BMMs were seeded onto the Osteo Assay strip well plates and infected with the lentivirus carrying PXR shRNA or the control lentivirus and then cultured in the presence of M-CSF and RANKL for 5 days with or without IPA (50 μM) treatment. F-actin was visualized using phalloidin staining, and three patterns of podosomes—including podosome clusters, actin rings, and podosome belts—were counted. (G, H) BMMs were treated as described in (E, F); the cells were then washed from the surface by using the 10% bleaching solution for 5 min. Resorption pits were captured with light microscopy and analyzed using Image J software. (I-L) BMMs were seeded on six-well plates and infected with the lentivirus carrying PXR shRNA or the control lentivirus and then cultured in the presence of M-CSF and RANKL for 5 days with or without IPA (50 uM) treatment. Relative mRNA expression of osteoclast-specific genes was quantified using qPCR. (M-R) BMMs were treated as described in (I-L). Protein levels of osteoclast-specific genes and PXR were determined using Western blot. * $P < 0.05$; ** $P < 0.01$; *** $P < 0.001$; NS, no significance.
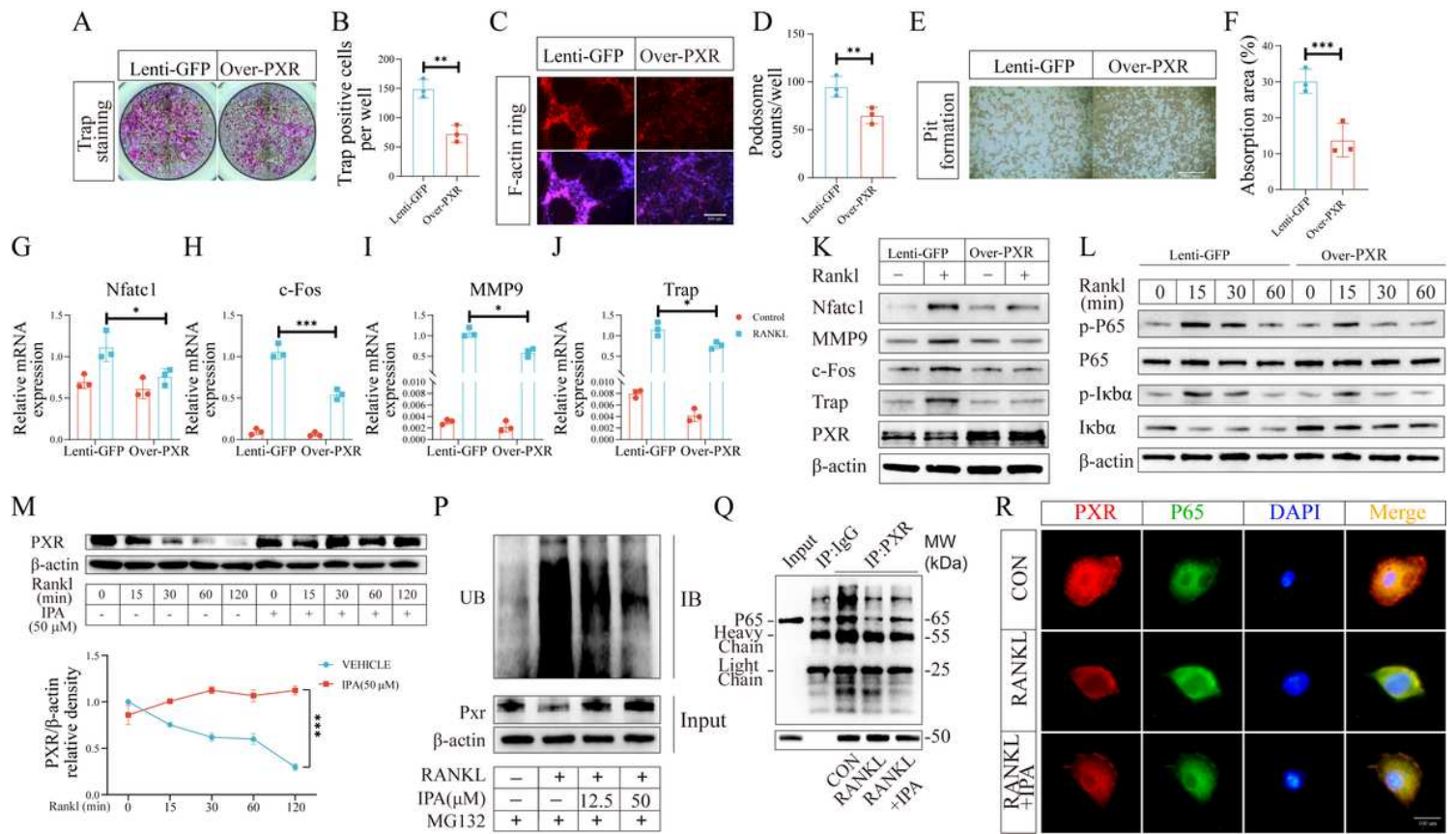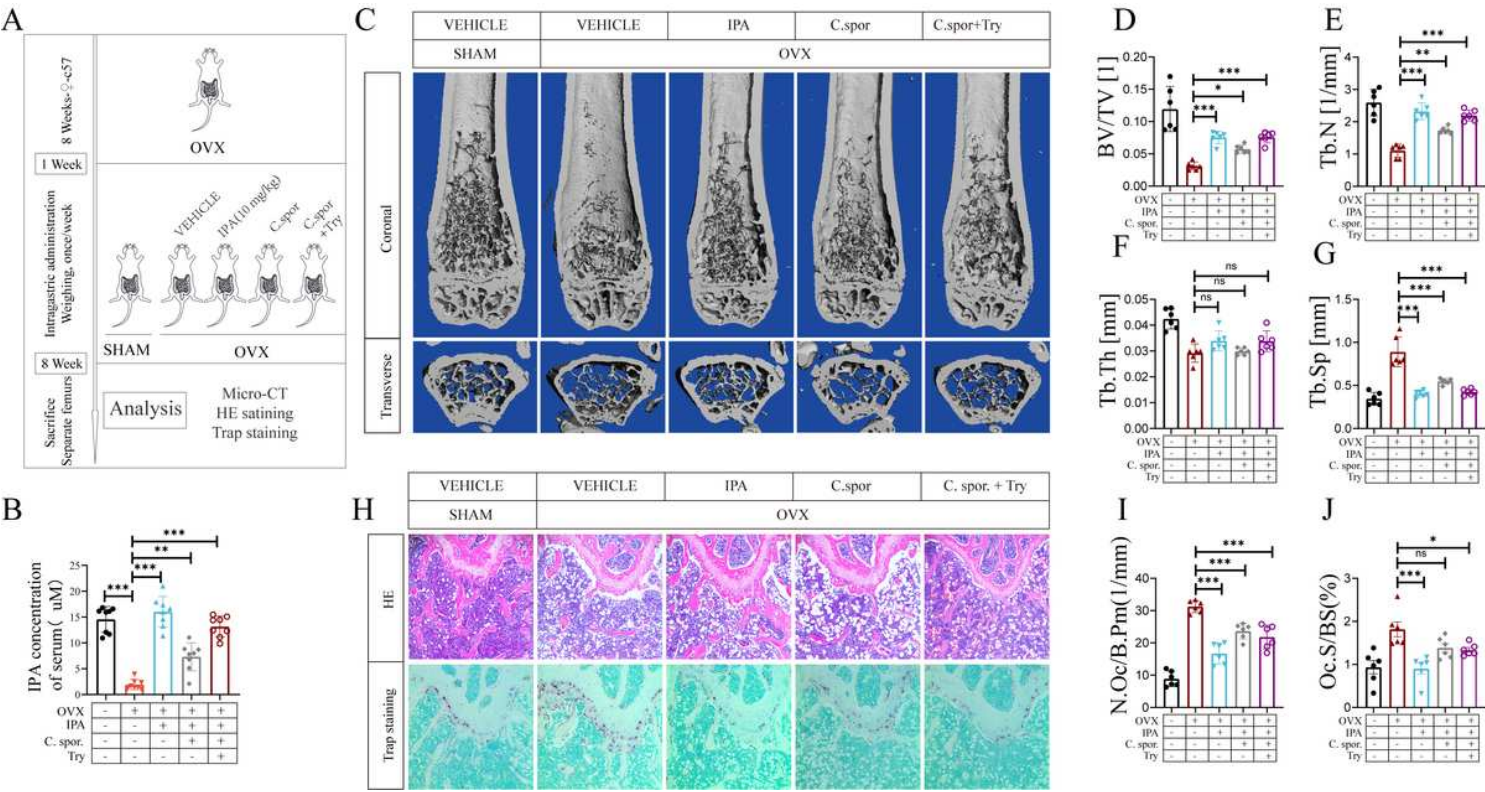
Figure 5

IPA suppresses PXR ubiquitination and anchors p65

(A, B) BMMs were infected with PXR-overexpressing lentivirus (over-PXR) or the GFP lentivirus (GFP) and then cultured in the presence of M-CSF and RANKL for 5 days. TRAP staining was performed, and TRAP-positive cells with three or more nuclei were counted as osteoclasts. (C, D) BMMs were seeded onto the Osteo Assay strip well plates and infected with lentivirus carrying Over-OXR or GFP and then cultured in the presence of M-CSF and RANKL for 5 days. F-actin staining was then performed, and three patterns of podosomes—podosome clusters, actin rings, and podosome belts—were counted. (E, F) BMMs were treated as described in (C, D); the cells were washed from the surface by using the 10% bleaching solution for 5 min. Resorption pits were captured with light microscopy and analyzed using Image J software. (G-J) BMMs were seeded onto six-well plates and infected with Over-PXR or GFP lentivirus and then cultured in the presence of M-CSF with or without stimulation of RANKL for 5 days. Relative mRNA expression of osteoclast-specific genes was quantified using qPCR. (K) BMMs were treated as described in (G-J). Protein expression of osteoclast-specific genes and PXR was determined using Western blot. (L) Western blot assay examined the activation of NF-kappa B signaling pathway after PXR over expression. (M) Protein levels of PXR after RANKL treatment were measured at indicated time points with or without IPA pretreatment. (P) BMMs were seeded on six-well plates and incubated with 30 ng/mL M-CSF and 75 ng/mL RANKL for 5 days; MG132 (10 μM) was added for the final 4 hours of incubation. Total-cell lysates were subjected to immunoprecipitation using anti-PXR antibody. Immunoprecipitates were separated by SDS-PAGE and immunoblotted using anti-ubiquitin antibody. (Q) BMMs were seeded on six-

well plates and incubated with 30 ng/mL M-CSF and 75 ng/mL RANKL for 5 days. Total-cell lysates were subjected to immunoprecipitation using anti-PXR antibody. Immunoprecipitates were separated by SDS-PAGE and immunoblotted using anti-p65 antibody. (R) Representative immunofluorescence images showing p65 (green), PXR (red), and nucleus (blue) in cells incubated with 30 ng/mL M-CSF and 75 ng/mL RANKL with or without IPA (50 uM). * P < 0.05; ** P < 0.01; *** P < 0.001; NS, no significance.

Figure 6

Both IPA supplement and *C. spor.* colonization protect mice against OVX-induced bone loss

(A) Schematic diagram of the animal study. (B) Serum concentrations of IPA in each group. (C) Representative 3D-reconstructed images of the distal femurs of mice in each group. (D-G) Quantitative analyses of bone structural parameters of the distal femurs, including bone volume/tissue volume (BV/TV), trabecular numbers (Tb.N), trabecular thickness (Tb.Th), and trabecular space (Tb.Sp). (H) Representative sections of the distal femurs visualized using H&E (scale bar = 1000 μm) and TRAP (scale bar = 1000 μm) staining. (I, J) Quantitative analyses of histomorphometric bone parameters, including N.Oc/B.Pm and Oc.S/BS, were performed. All data are presented as mean ± SEM. * P < 0.05; ** P < 0.01; *** P < 0.001; NS, no significance.
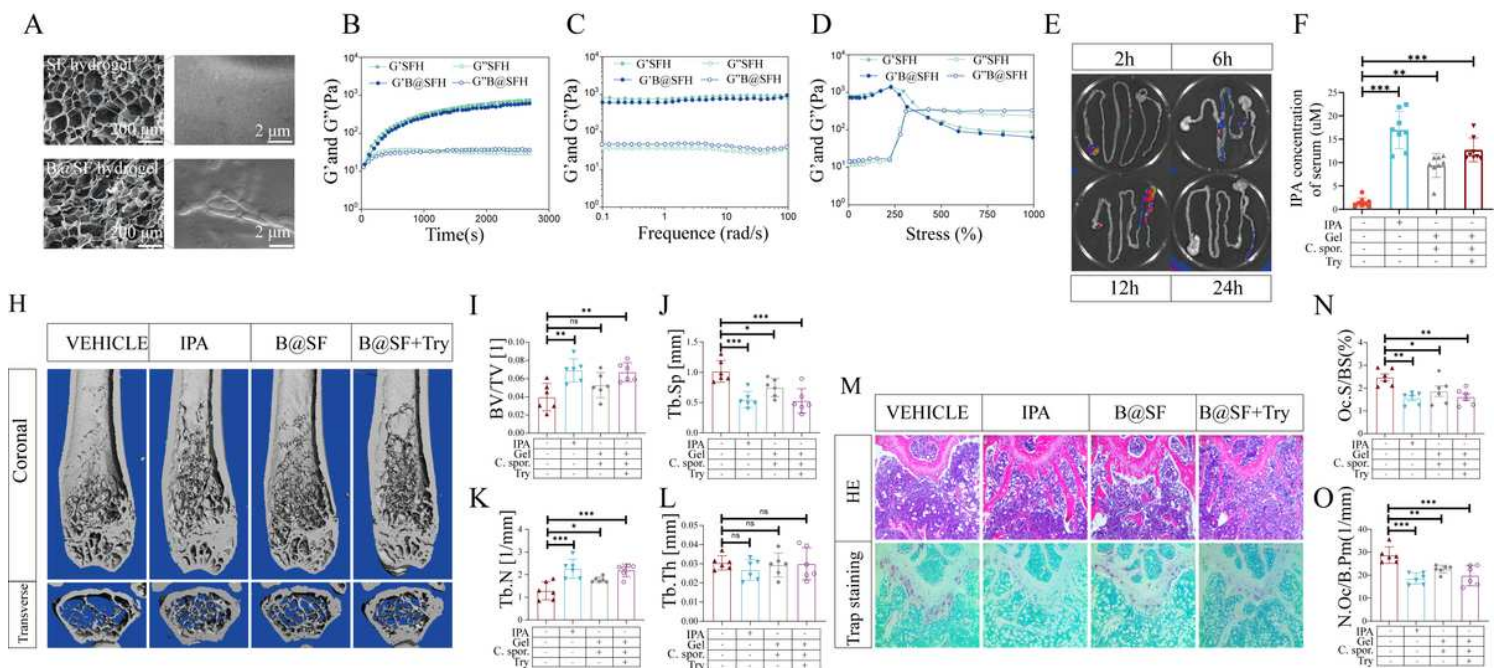
Figure 7

C. spor.-encapsulated SF hydrogel treatment inhibits OVX-induced bone loss

(A) SEM of silk fibroin (SF) hydrogel and bacteria-encapsulated SF (B@SF) hydrogel. Results of time sweep (B), frequency sweep (C), and strain sweep (D) showed no difference between the SF and B@SF hydrogels. (E) *In vivo* intestinal retention effect of SF and B@SF hydrogels. (F) Serum concentrations of IPA in each group. (H) Representative 3D-reconstructed images of the distal femurs of mice in each group. (I-L) Quantitative analyses of bone structural parameters of the distal femurs, including BV/TV, Tb.N, Tb.Th, and Tb.Sp. (M) Representative sections of the distal femurs visualized using H&E (scale bar = 1000 μm) and TRAP (scale bar = 1000 μm) staining. (N, O) Quantitative analyses of histomorphometric bone parameters, including N.Oc/B.Pm and Oc.S/BS, were performed. All data are presented as mean ± SEM. * P < 0.05; ** P < 0.01; *** P < 0.001; NS, no significance.

Supplementary Files

This is a list of supplementary files associated with this preprint. Click to download.

- 08032023SupplementPRP.docx